Journal of Colloid and Interface Science 608 (2022) 1051–1063

Contents lists available at ScienceDirect

Journal of Colloid and Interface Science

journal homepage: www.elsevier.com/locate/jcis

Self-assembly hybridization of COFs and g-C_3N_4: Decipher the charge transfer channel for enhanced photocatalytic activity

Han Wang [a,c], Eydhah Almatrafi [c], Ziwei Wang [a], Yang Yang [a], Ting Xiong [b], Hanbo Yu [a], Hong Qin [a], Hailan Yang [a], Yangzhuo He [a], Chenyun Zhou, Methodology, Writing-review&editing [a,c], Guangming Zeng, Conceptualization, Formal analysis, Investigation, Methodology, Visualization, Writing-review&editing [a,*], Piao Xu [a,c,*]

[a] *College of Environmental Science and Engineering, Hunan University and Key Laboratory of Environmental Biology and Pollution Control, Ministry of Education (Hunan University), Changsha 410082, PR China*

[b] *Institute of Big Data and Internet Innovation, Hunan University of Technology and Business, Changsha 410205, PR China*

[c] *Center of Research Excellence in Renewable Energy and Power Systems, Center of Excellence in Desalination Technology, Department of Mechanical Engineering, Faculty of Engineering-Rabigh, King Abdulaziz University, Jeddah 21589, Saudi Arabia*

HIGHLIGHTS

- A metal-free self-assembled covalent organic framework (TpMa)/ g-C_3N_4 (CN) heterojunction was prepared via π-π interaction.
- A built-in electric field was formed at the interface of TpMa and CN.
- The introduction of donor–acceptor conjugated TpMa leads to the enlarged visible-light absorption of CN.
- TpMa/CN shows enhanced photocatalytic activity under visible-light irradiation.

GRAPHICAL ABSTRACT

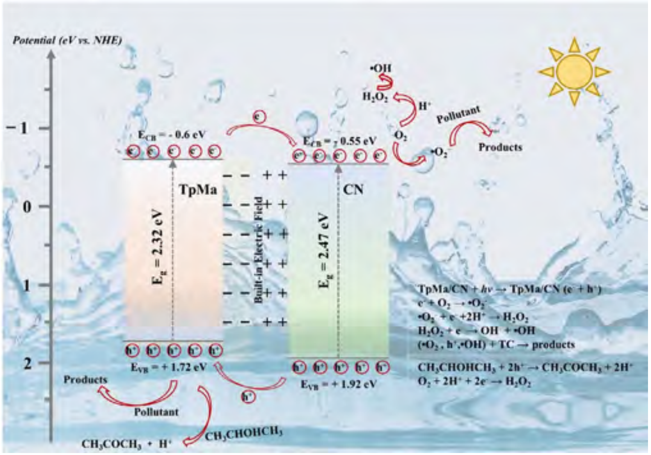

ARTICLE INFO

Article history:
Received 31 August 2021
Revised 30 September 2021
Accepted 8 October 2021
Available online 12 October 2021

Keywords:
Graphitic carbon nitride
Covalent organic framework
Photocatalysis
Electric field
Self-assembling

ABSTRACT

Organic semiconductors have been recognized as a new generation of photocatalysts for pollutants degradation and energy production. Herein, organic heterojunction (TpMa/CN) consisting of carbon nitride and β-ketoenamine-based covalent organic framework is fabricated via a controllable self-assembly approach. The as-prepared TpMa/CN heterojunctions show enlarged visible-light absorption. The optimum TpMa/CN-5 photocatalyst achieves the highest photocatalytic activity towards tetracycline degradation, and its photocatalytic degradation rate is improved by 2.3 and 4.3 times than TpMa and CN, respectively. As a multifunctional photocatalyst, TpMa/CN-5 sample also shows remarkable photocatalytic activity for hydrogen peroxide production (880.494 μM h^{-1}), which is 49 times higher than that of CN. Experimental and theoretical investigations indicate that a built-in electric field is formed at the interface of composite, which enables an accelerated charge transfer and separation. This work develops an effective strategy to design difunctional photocatalyst and deciphers the electronic properties and

---

* Corresponding authors.
E-mail addresses: zgming@hnu.edu.cn (G. Zeng), piaoxu@hnu.edu.cn (P. Xu).

https://doi.org/10.1016/j.jcis.2021.10.036

mechanisms of g-C_3N_4-based organic photocatalysts, which spurs further interests for organic heterojunction photocatalysts in the future.

1. Introduction

With the rapid industrialization and urbanization, energy shortage and environmental pollution are of great concern over the years. Photocatalysis converts abundant and inexhaustible solar energy into valuable chemicals and fuels, representinfvg an operative and scalable technology [1–3]. Organic photocatalysts, especially conjugated polymers, owning properties of metal-free, processability and tunability, have been regarded as a new complement to inorganic semiconductor photocatalysts [4–7]. Among the fascinating conjugated polymers, polymer carbon nitride (CN), featured by low cost, high stability and suitable band gap structure, is the most investigated visible-light-responsive organic photocatalyst [8–11]. However, potential shortcomings and obstacles of pristine g-C_3N_4 hinder the development, including low electrical conductivity, high recombination rate of charge carriers and limited visible light adsorption (ca. 460 nm) [12]. Several strategies have been explored to make up for the defects, such as copolymerization [13], element doping [14] and heterojunction construction [15]. Among them, great efforts have been made in developing g-C_3N_4-based heterostructure photocatalysts with promoted charge separation and extended visible-light absorption for improved photocatalytic activity [16]. Especially, designing g-C_3N_4-based heterojunction with donor–acceptor (D-A) conjugated polymers holds great promise [17]. The formation of intramolecular charge transfer (ICT) in D-A structure from donor to acceptor units leads to the enhanced visible-light absorption and endows the adjustment of energy levels.

Covalent organic frameworks (COFs), as a newly developed crystalline organic polymer, show tremendous potential on photocatalysis [18–19]. COFs synthesized from molecular building blocks endow them with chemical tunability to realize the design of targeted porous structures and special properties related to photocatalytic reactions such as light-harvesting capability, electron-hole separation and transfer. And the large surface area ensures the accessible catalytic sites. Moreover, the extended π-conjugated structures in COFs could accelerate charge carrier separation along in-plane and out-plane stacking direction. Since the pioneering study of Lotsch and co-workers that reported a hydrazine-based TFPT-COF with high photocatalytic hydrogen evolution efficiency [20], the research of COF-based photocatalysts have been developed [21–22]. However, the starting materials of COFs usually cost high and need complex synthesis, which greatly hampers their large-scale application. Constructing heterojunctions based on COFs and economical CN could be an effective method. Yan et al. synthesized a COF-modified g-C_3N_4 with imine linkage which showed a higher photocatalytic H_2 evolution rate owing to the accelerated photoinduced charge carriers separation and migration originated from the difference band levels of g-C_3N_4 and COF as well as the transfer route along the imine linkage [23]. Hou et al. constructed several CuPor-Ph-COF/g-C_3N_4 photocatalysts by a facile liquid-assisted grinding method. CuPor-Ph-COF/g-C_3N_4 composites showed enhanced degradation efficiency of rhodamine B under visible light resulting from the improved photogenerated charge separation [24]. While most of the recent studies focus on the photocatalytic activities of the COF-based photocatalysts, the investigation of the internal essence on the interfacial charge transfer in COFs/g-C_3N_4 heterojunction, especially for the microscopic charge behavior, is limited.

Herein, the donor–acceptor conjugated COF (TpMa), based on 1, 3, 5-triformylphloroglucinol (Tp) aldehyde and melamine (Ma), is selected to combine with g-C_3N_4 to fabricate a type II heterojunction (TpMa/CN) for improved photocatalytic performance. With the existence of the π-π interactions, TpMa could be introduced into g-C_3N_4 via self-assembly [25], and an effective interfacial electron transfer channel could be built driven by the internal electric field. Specifically, electron-donor β-ketoenamine and electron-acceptor triazine units in TpMa COF can cause intramolecular charge transfer, thereby facilitating excitons separation. And TpMa keeps stable under light irradiation considering the existence of the irreversible β-ketoenamine formation [26]. Previous study demonstrated that TpMa with C_3N_4 constituent shows potential visible-light photocatalytic activity [27]. As expected, the resulting TpMa/CN shows extended light absorption and inhibited recombination rate of photogenerated charge carrier. For photocatalytic applications, enhanced photocatalytic tetracycline (TC) degradation and hydrogen peroxide (H_2O_2) production are realized. Furthermore, photoelectrochemical experiments and density functional theory (DFT) calculations are applied to better understand the photocatalytic mechanism of TpMa/CN heterostructures. This study comprehensively deciphers the underlying mechanisms, including the electronic properties and photocatalytic behavior, of the polymer heterojunction photocatalysts, which will provide new inspiration in designing highly efficient organic photocatalysts.

2. Experimental section

2.1. Synthesis

TpMa was synthesized via a solvothermal process according to the previous report [28]. Generally, 0.3 mmol 1, 3, 5-triformylphloroglucinol (Tp) and 0.3 mmol Melamine (Ma) were added in the solvent of N, N-dimethylacetamide (DMAc) and dimethyl sulfoxide (DMSO) (2:1, v: v) with a certain amount of aqueous acetic acid. The mixture was ultrasonicated to disperse homogeneously, and degassed through three successive freeze–pumpthaw cycles. Then, the mixture was heated at 120 °C for 3 days with the tube sealed. The obtained yellow products were filtered out and washed with excess DMAc and water. Finally, the resulting TpMa was dried in a vacuum oven.

Raw g-C_3N_4 (CN) was prepared through a traditional calcination method [29]. In a typical synthesis, 8 g of Ma was placed in a covered crucible and kept at 550 °C for 4 h with a heating rate of 2.3 °C min^{-1}. The resulting yellow product was grinded, washed, and then dried.

The TpMa/CN photocatalysts were prepared by an in-situ self-assembly method based on π-π interaction. First, the as-prepared CN was dispersed into DMSO, and ultrasonicated for 2 h to form dispersive CN solution. Then, a given mass of TpMa was added and continued to ultrasonic for another 2 h. Subsequently, the mixture was stirred for 24 h under room temperature to strengthen the interaction. The products were filtered out and washed with water and ethyl alcohol, and then dried in vacuum oven at 80 °C. CN photocatalyst with different TpMa content was designated as TpMa/CN-X, in which “X%” represented the mass percentage of TpMa to CN (X = 1, 5, 10, 15, 25).

2.2. Photocatalytic degradation experiments

In general, a model contaminant tetracycline (TC) was chosen, and a light source of a 300 W Xe lamp (CEL-HXF300, Ceaulight, λ > 420 nm) was used in all experiments. Photocatalyst (50 mg) was added in TC aqueous solution (50 mL, 20 mg L^{-1}) with ultrasonic dispersion. Then adsorption–desorption equilibrium experiment was conducted by stirring the resulting mixture in the dark for 60 min before irradiation. After that, the mixture was put under the light source. At a given time, sample was collected for analyses. As for the stability analysis, the remaining solution was centrifuged, and the products were gathered, washed and dried for further cycle experiment. The UV–vis spectrophotometer was employed to detect the concentration of TC at the characteristic absorption wavelength of 357 nm. The total organic carbon (TOC) was record by a TOC analyzer (Analytikjena multi N/C 2100).

2.3. Photocatalytic H_2O_2 production test

The photocatalytic H_2O_2 production test was performed by adding each photocatalyst (25 mg) in the IPA (5 mL) and deionized water (45 mL) mixture in which IPA acted as the electron and proton donor. Adsorption-desorption equilibrium experiment was conducted before irradiation. The mixture was first dispersed by ultrasonic for several minutes and stirred with O_2 bubbling in the dark for 60 min. Then, the mixture was exposed to the light source. At a given time, a certain amount of solution was collected and filtrated. Iodometry was employed to detect the amount of H_2O_2 [30]. Typically, potassium hydrogen phthalate aqueous solution ($C_8H_5KO_4$, 0.1 M, 1 mL) and potassium iodide aqueous solution (KI, 0.4 M, 1 mL) were added into the resulting solution in sequence, and stood for 30 min. The concentration of I^{3-} was then analyzed by UV-2700 spectrophotometer with an absorbance peak at 350 nm·H_2O_2 molecules could react with I^- to generate I^{3-} under acidic condition, thereby obtaining the amount of H_2O_2.

3. Results and discussion

3.1. Photocatalysts characterization

The synthetic process of TpMa/CN is illustrated in Scheme 1. CN was obtained from traditional calcination method, which presented an aggregated crystal stacking layer with smooth surface, as shown in Fig. 1a and Fig. 1d. The TpMa was prepared under solvothermal conditions. The resulted TpMa exhibited a fibrous nanobelt morphology with a diameter of about 116.1 nm (Fig. 1b, Fig. 1e, and Fig. S1). The stacking layered CN was under a DMSO assisted ultrasonication to obtain few-layer CN nanosheets, and then added TpMa. With self-assembly via π-π interaction [31], TpMa was found to adhere to the surface of CN, which was verified by the SEM and TEM characterization (Fig. 1c and Fig. 1f). The as-prepared heterojunctions well-preserved each original structure and further established a good interfacial contact, which was beneficial to the construction of built-in electric field.

The crystal structures of samples were determined by XRD analyses. As depicted in Fig. S2a, CN and TpMa exhibit a similar characteristic peak at around 2θ = 27.5°, which can be assigned to the representative (002) planes, corresponding to the interlayer stacking of conjugated aromatic planes. Distinctively, the CN features by the characteristic peak at 13.1°, indicating the existence of repeated in-plane heptazine units, while the TpMa displays a characteristic peak of 9.7°, originating from the repetition of triazine units [28,32]. As compared with CN, similar diffraction patterns of TpMa/CN heterojunctions suggest that coupling with TpMa does not change the main structure of CN. However, slight decrease of diffraction peak at 27.5° is observed after coupling with an increasing amount of TpMa, which can be ascribed to their interaction. No obvious diffraction peaks of TpMa can be observed in the hybrids. Two crucial aspects should be taken into accounts: (i) TpMa and CN both have diffraction peak around 27.5° and the inherently weaker diffraction peak of TpMa would be covered up, and (ii) the amount of TpMa was a little as compared to CN. The FTIR spectroscopy was also utilized to analyze the structure of samples (Fig. S2b and Fig. S3). Similar framework was found in the samples. The peak at 807 cm^{-1} is corresponding to the out-of-plane bending mode of tri-s-triazine-based structure, and the peaks located at 1200 ~ 1700 cm^{-1} are ascribed to the typical C—N heterocycles [33]. No distinct peaks of CN alter, further implying the main structure of CN and the small amount of TpMa on the samples.

Meanwhile, XPS was further used to analyze the surface information of the samples. The total survey XPS spectra of CN, TpMa and TpMa/CN-5 in Fig. 2a displays the signal of C, N and O elements, which is corresponding well to the peaks at around 288 eV, 398 eV and 531 eV, respectively [34]. The C/N and O/N atom ratios for CN, TpMa and TpMa/CN-5 were also listed in Table S1b. Noted that a slight increase of C/N and O/N atom ratios is observed in the XPS spectra of TpMa/CN-5, which is in good agreement with element analysis (Table S1a) and further proves the successful construction of the heterojunction. Besides, the high resolution XPS spectra of CN, TpMa and TpMa/CN-5 are respectively displayed in Fig. 2b-d and Fig. S4. As shown in Fig. 2b, the CN exhibits peaks at 289.1 eV, 288.1 eV, 286.8 eV, and 284.8 eV, which can be ascribed to C—O, N=C—N, C—H and C—C. As compared to CN, the binding energies of these four C-related peaks exhibit a negative shift indicating an electron rearrangement after hybridization. Notably, a new peak at 286.6 eV is observed, which is assigned to C=O bond originated from TpMa [35]. The characteristic peak of C=O in TpMa/CN-5 shows a negative shift as compared to that in TpMa, which demonstrates an electron transfer between TpMa and CN. The high-resolution N1s was also analyzed. Both the spectrum of CN and TpMa/CN-5 could be deconvoluted into three N species, which are centered at 400.9 ~ 400.8 eV, 399.8 ~ 399.9 eV, and 398.6 ~ 398.7 eV, correlated with the terminal C—N—H amino functions, the inner atoms bonded with the N-$(C)_3$, and the *sp*^{2}-bonded nitrogen in s-triazine ring (C=N-C), respectively [15]. In reverse to the C 1 s spectra, the *N*-related peaks exhibit a slight positive shift in TpMa/CN-5 as compared that of CN, implying the decrease of electron density. As shown in the high-resolution O1s (Fig. 2d), the peaks at around 533.3 eV, 532.4 eV, and 531.5 eV could be ascribed to inevitable O doping during the thermal polymerization process in air [36–37]. As for the additional peak at 530.3 eV in TpMa/CN-5, it corresponded to the C=O group on TpMa. These results further confirmed the successful synthesis of TpMa/CN heterostructure.

In addition, the specific surface area of photocatalysts has a great influence on their performance considering the active centers. N_2 adsorption–desorption measurements were further employed to analyze the surface area of CN and TpMa/CN-5. As shown in Fig. 3a, Fig. S5 and Table S2, the CN, TpMa and TpMa/CN-5 are mesoporous materials as proved by a type IV isotherm with an H1 type hysteresis loop, and the BET surface area is determined to be 11.90, 106.1 and 15.45 m^2 g^{-1}, respectively. A slight increase of the BET surface area of TpMa/CN-5 as compared to CN demonstrates that more adsorbent active sites can be provided. The pore size of TpMa/CN-5 (27.19 nm) is smaller than that of CN (31.80 nm), which could be ascribed to the in-suit stacked TpMa that overlay partial surface of CN. Thermogravimetric analysis (TGA) under N_2 atmosphere shows the thermal stability of TpMa/CN up to 400 °C (Fig. S6).

The light absorption property of the samples was then investigated by UV–vis DRS and depicted in Fig. 3b. The CN exhibits a lim-

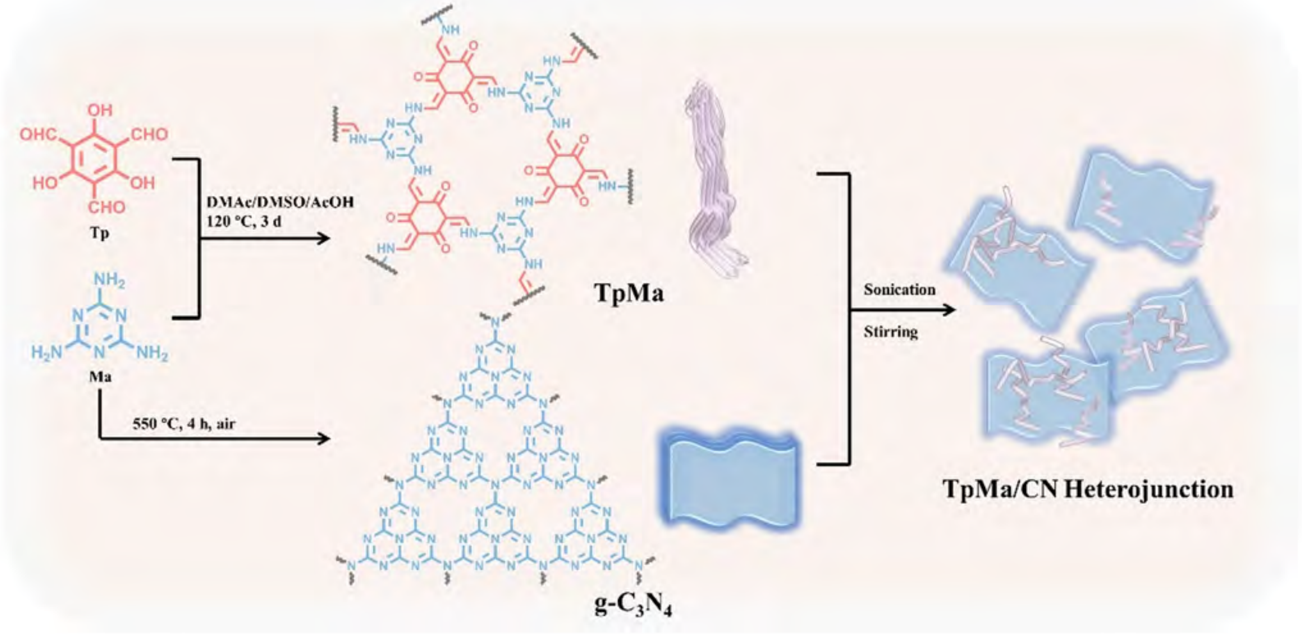

Scheme 1. Process of the synthesis of TpMa/g-C_3N_4 (TpMa/CN) heterojunctions.

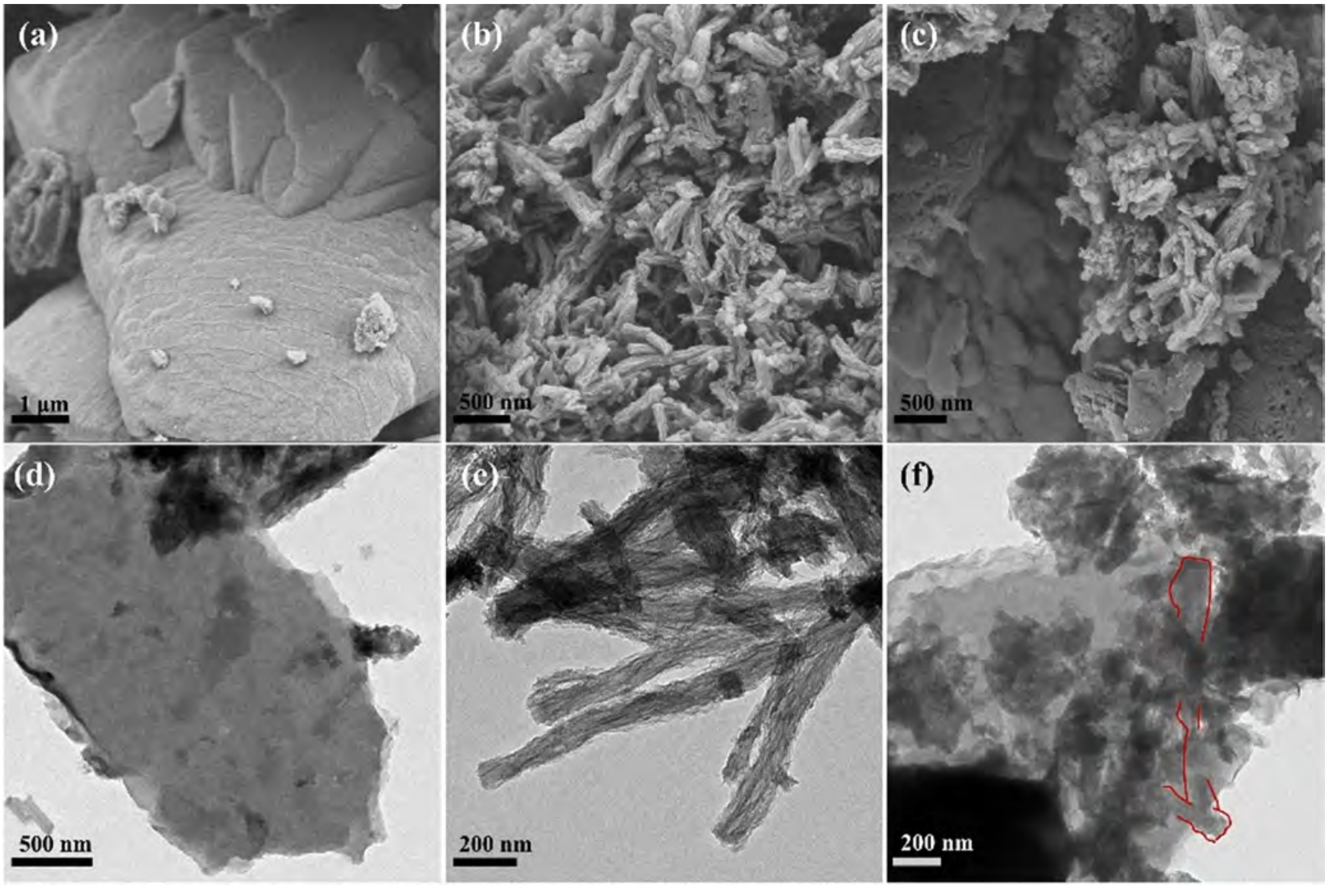

Fig. 1. SEM and TEM images of CN (a, d), TpMa (b, e), and TpMa/CN-25 (c, f).

ited light absorption of around 460–470 nm, whereas the TpMa presents an enlarged visible light absorption ($\lambda > 650$ nm) due to the D-A conjugated skeleton, which has an ICT from D to A and causes a broaden absorption spectrum range [38]. The absorption edge of TpMa/CN heterojunctions, though has a blue-shift as compared to TpMa, is larger than that of CN. The strengthened optical

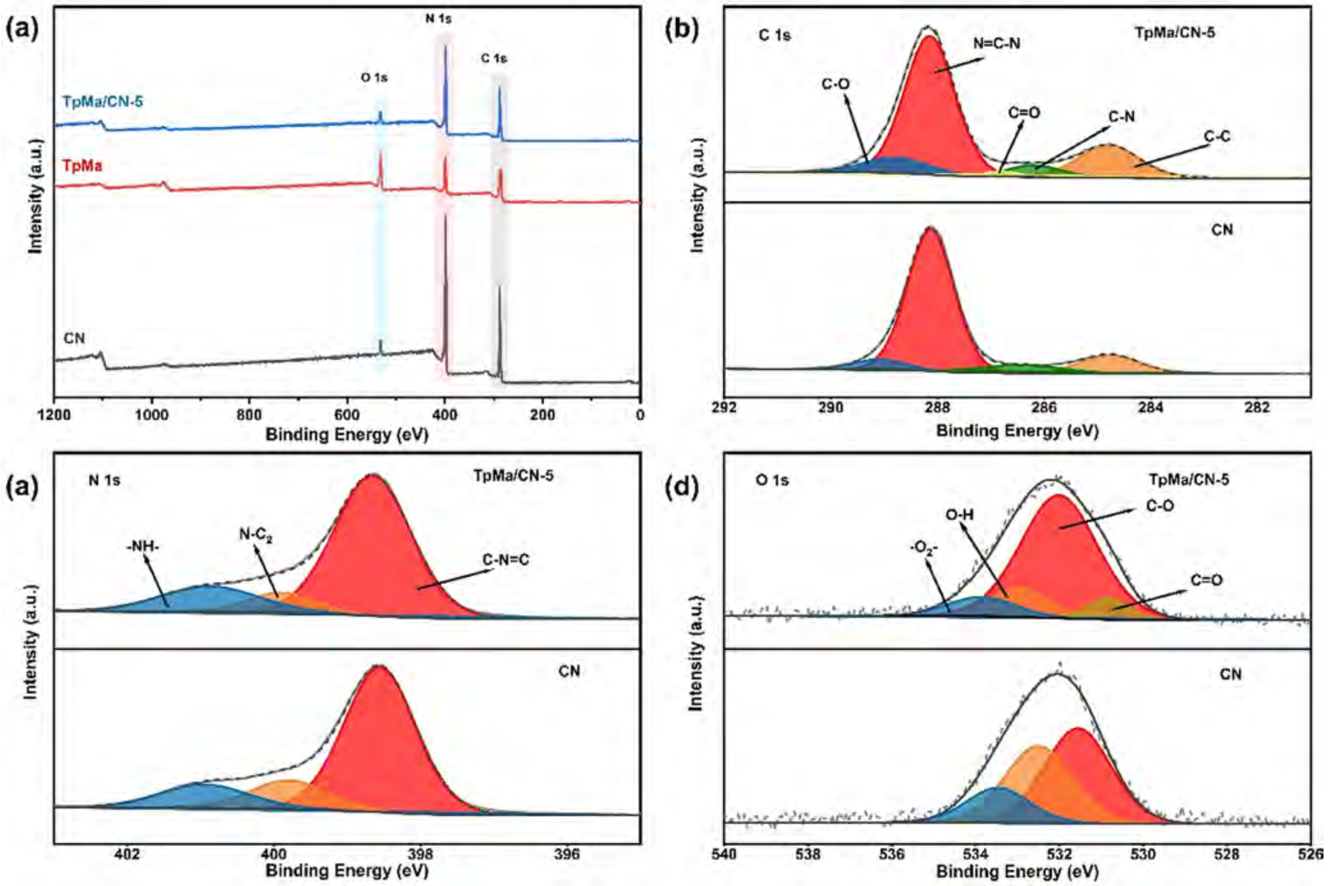

Fig. 2. XPS spectra for (a) total survey, (b) C 1 s, (c) N 1 s and (d) O 1 s of CN and TpMa/CN-5 samples.

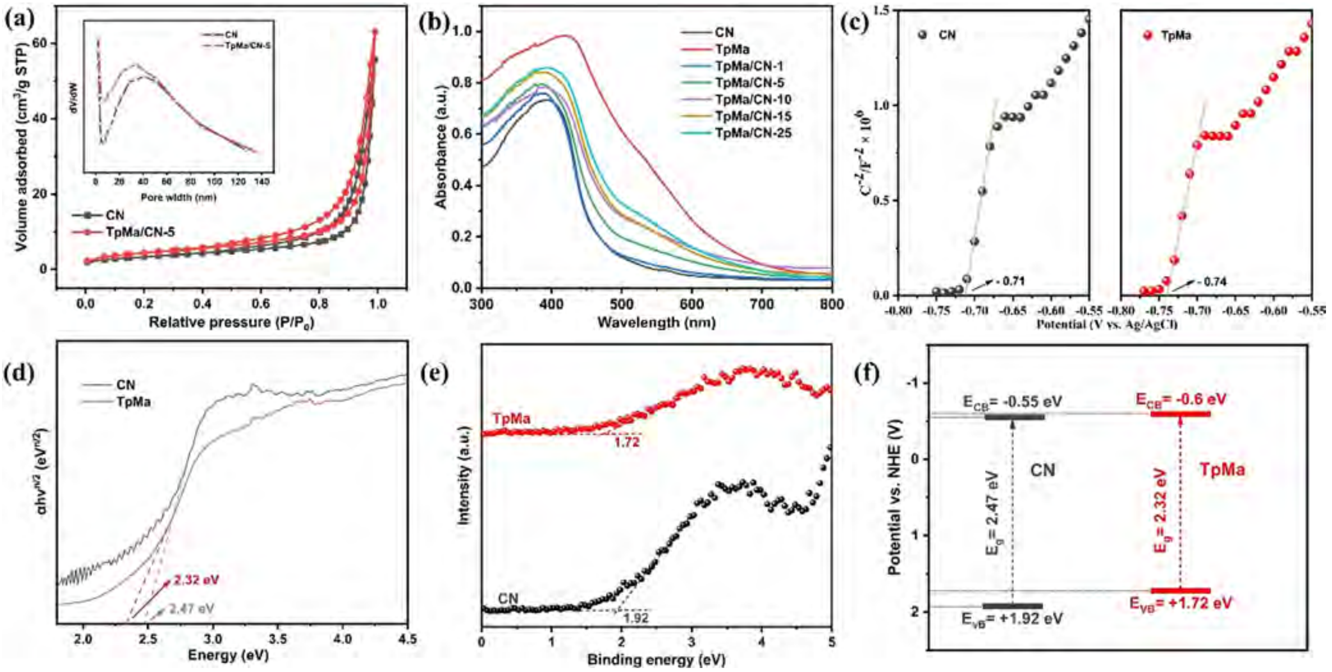

Fig. 3. (a) N_2 adsorption–desorption isotherms and the pore size distribution curves (insert) for CN and TpMa/CN-5; (b) UV–vis DRS for CN, TpMa, TpMa/CN-1, TpMa/CN-5, and TpMa/CN-10; Mott-Schottky plots (c), the Tauc plots (d), XPS valence band spectra (e) and band structure diagrams (f) for CN and TpMa/CN-5.

adsorption of the samples demonstrated the successful synthesis of TpMa/CN heterostructures with improved visible light absorption. Additionally, the electronic energy level of CN and TpMa was analyzed by Mott-Schottky (MS) measurements and valence band (VB) XPS spectra. As depicted in Fig. 3c, CN and TpMa are both *n*-type semiconductor, and the flat-band potential (U_{fb}) of CN and TpMa is determined to be −0.71 and −0.74 V versus NHE, respectively. Notably, the conduction band (CB) of *n*-type semiconductors is about 0–0.2 V deeper than U_{fb}. The energy band edge (E_g) of CN and TpMa was determined by the Kubelka-Munk equation (Eq. (1)):

$$\alpha h\upsilon = A(h\upsilon - E_g)^{n/2} \tag{1}$$

where A is a constant; α, h, and ν represent the absorption coefficient, light frequency and Planck's constant, respectively. The value of n is based on the electronic transition type of semiconductors. Thus, n = 1 for indirect transition of CN while n = 4 for direct transition of TpMa [13,35]. The band gap of CN and TpMa is calculated to be 2.47 and 2.32 eV, respectively (Fig. 3d). The TpMa possesses a narrower band gap than CN due to the photoelectron shift platform based on the conjugated system of TpMa [27]. The VB positions of CN and TpMa were further investigated through the VB XPS technique, which are found to be 1.92 and 1.72 eV, respectively, as shown in Fig. 3e. In general, the electronic energy level structure of CN and TpMa was depicted in Fig. 3f, where the CB potential of CN and TpMa is determined to be –0.55 and –0.6 eV based on the equation (Eq. (2)), which are in accordance with the MS measurements:

$$E_{CB} = E_{VB} - E_g \tag{2}$$

where E_g, E_{CB} and E_{VB} represent the band gap energy, CB potential and VB potential, respectively.

It was well-understood that the separation and migration of photogenerated carriers played crucial roles in photocatalysis [39–40]. Herein, transient photocurrent response curves as well as electrochemical impedance spectroscopy (EIS) were conducted to analyze the interfacial charge transfer behaviors. As shown in Fig. 4a, the lowest current density is found in the CN sample, which could be ascribed to the rapid photo-generated electron-hole recombination. As compared with CN, higher current density is presented in the TpMa sample, while the highest current density is achieved in the TpMa/CN-5 due to the interfacial charge transfer between TpMa and CN. Additionally, Fig. 4b shows the EIS analysis of CN, TpMa and TpMa/CN-5, where TpMa/CN-5 with a smaller arc radius indicates a reduced charge transfer resistance and an accelerated charge transfer rate. Furthermore, Fig. 4c shows the bode phase spectra of the samples, a slightly lower frequency of TpMa/CN-5 is observed as compared to that of CN, implying an enhanced charge transfer process. In order to specify the charge behavior within photocatalysts, the photoluminescence tests were conducted. As exhibited in Fig. S7, TpMa/CN-5 photocatalyst presents a lower fluorescence intensity than CN, demonstrating the dis-

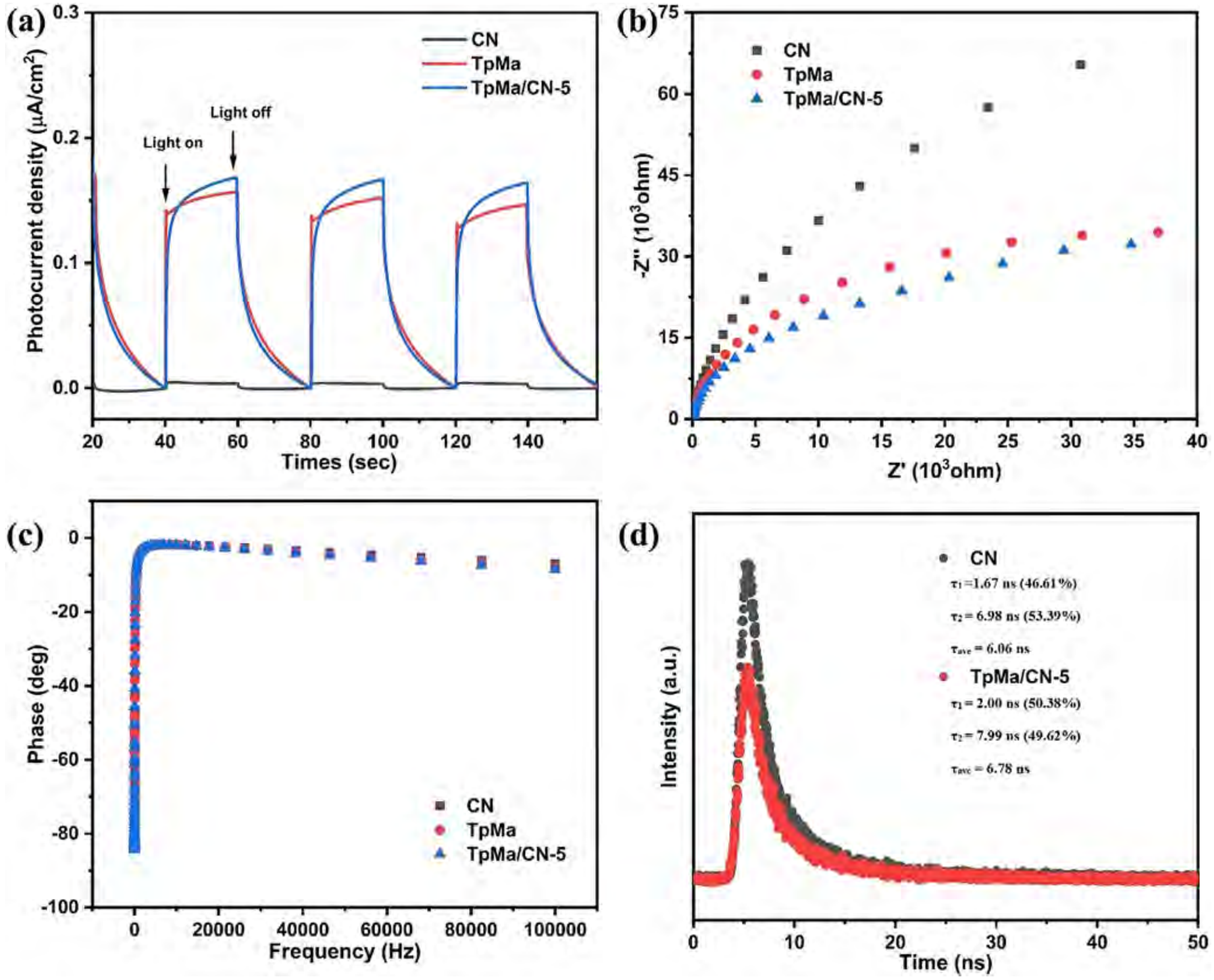

Fig. 4. (a) Transient photocurrent response curves, (b) EIS Nyquist plots and (c) Bode phase spectra of CN, TpMa and TpMa/CN-5. (d) Time-resolved photoluminescence decay spectra of CN and TpMa/CN-5.

tinctly reduced population of excitons. Time-resolved photoluminescence decay spectra was further performed to verify the above viewpoint and displayed in Fig. 4d. The average fluorescence lifetimes of CN and TpMa/CN-5 were 6.06 and 6.78 ns, respectively. It can be inferred that TpMa/CN-5 can profit from TpMa, enabling the rapid charge carrier transfer and thereby inhibiting the recombination [41–42].

3.2. Photocatalytic activity

As a proof-of-concept application, TpMa/CN heterojunctions were first used as photocatalysts for TC degradation. Adsorption-desorption equilibrium experiments were conducted before visible-light irradiation (Fig. S8), and then the samples were exposed to visible light irradiation. As presented in Fig. 5a-b, negligible photolysis of TC is observed without photocatalysts under 60 min visible-light irradiation, and only 31% and 60% of TC can be photodegraded by CN and TpMa, respectively. Delightfully, TpMa/CN heterojunctions show enhanced photocatalytic decomposition efficiency as compared to CN and TpMa. Among them, TpMa/CN-5 displays the highest photocatalytic degradation efficiency (82%). The increased photocatalytic performance may be ascribed to the existence of built-in electronic field at the interface of CN and TpMa, which could promote the photoinduced carrier transport, reduce the charge carrier recombination rate. Nevertheless, the photocatalytic degradation efficiency of TC is decreased as the increase of the mass ratio of TpMa from 5% to 25%. The mass agglomeration of TpMa would weaken the crystal structure of CN as evidenced by XRD characterization above (Fig. S2a), and excessive TpMa may cause depressed light harvesting and cover the active spots of CN. In addition, the value of the apparent rate constant (k) for TC degradation was calculated via the simulated pseudo-first-order kinetic model based on the photodegradation experimental data. As displayed in Fig. 5c, the k value of TpMa/CN-5 is 0.02620, which is ca. 2.3 and 4.3 times higher than that of TpMa and CN, respectively. In addition, the comparison for TC degradation with other metal-free g-C_3N_4-based heterojunction photocatalysts is provided in Table S3, and TpMa/CN-5 exhibits excellent or tolerable activity evaluated by the reaction time, TC removal and rate constant. Thus, the successful introduction of TpMa is able to improve the photoactivity of CN, which could be ascribed to the accelerated photogenerated charge transfer and separation at the interface of TpMa and CN.

The total organic carbon (TOC) analysis was further used to evaluate the mineralization ability of TpMa/CN-5. As depicted in Fig. S10, the mineralization efficiency of TC reaches 34.5% within 120 min visible light irradiation, which is higher than that of CN. The incorporation of TpMa and CN could promote the mineraliza-

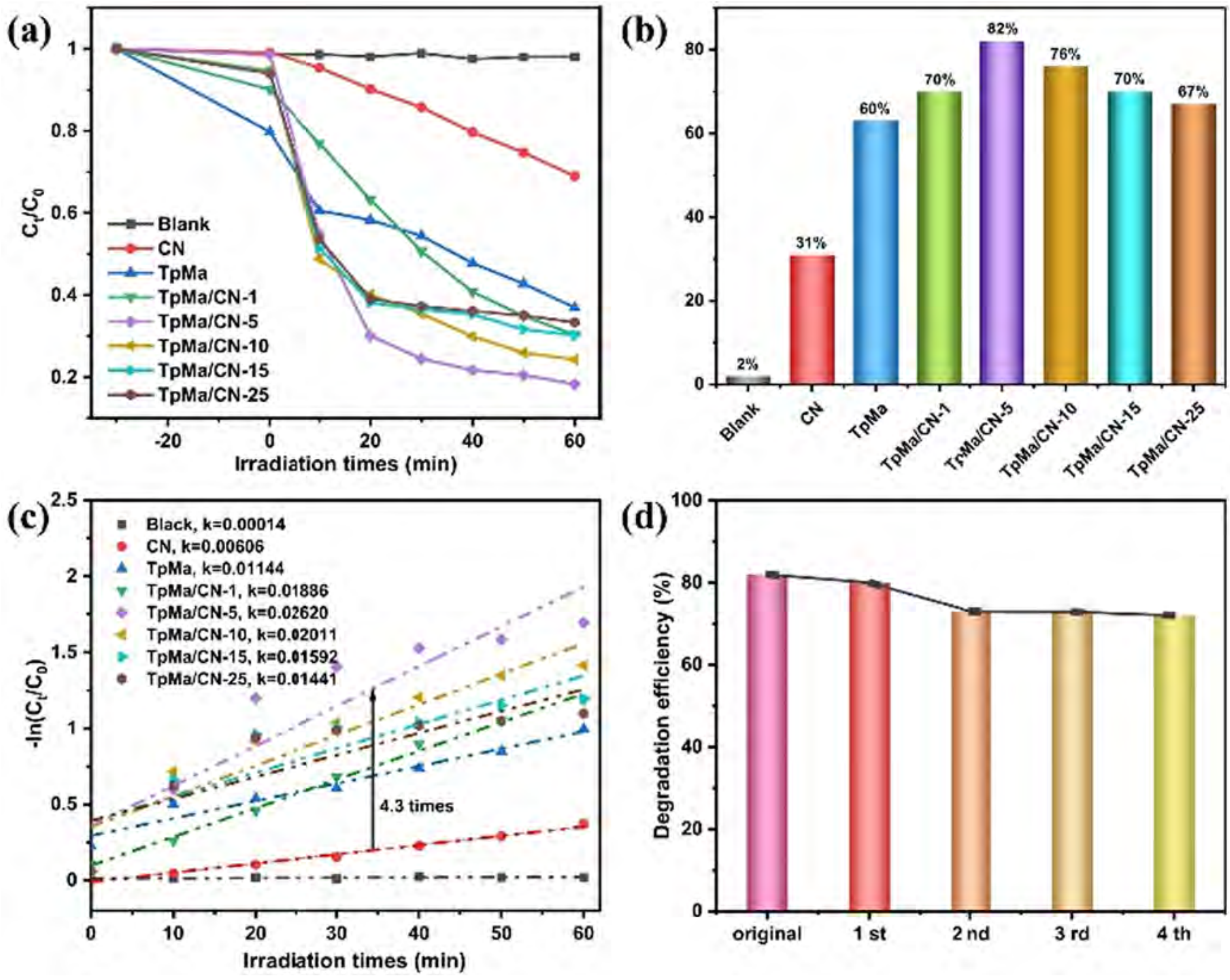

Fig. 5. (a) Time-dependent photocatalytic degradation, (b) degradation efficiencies, and (c) corresponding apparent rate constants over different samples; (d) Cycling measurement over TpMa/CN-5 photocatalyst.

tion process of TC to small intermediates, CO_2 and H_2O. Besides, the cycling experiments were conducted to reveal the recyclability and physicochemical stability of the TpMa/CN-5 in the TC photocatalytic degradation. As shown in Fig. 5, the activity of TpMa/CN-5 displays a slightly decrease while 73% degradation efficiency well-retained after four cycles. Moreover, the XRD and FTIR spectra of TpMa/CN-5 before and after irradiation are presented in Fig. S11, no clear change is found, indicating the retainment of the crystal and phase structures. The above results demonstrate that TpMa/CN-5 is stable in the photocatalytic TC degradation.

To better understand the reaction mechanism and main active species produced in the process of photocatalytic degradation, radical-trapping experiments and ESR analysis were studied. EDTA-2Na, IPA and TEMPOL were used as the quenchers of h^+, •OH and $\bullet O_2^-$, respectively. As depicted in Fig. 6a-b, the degradation efficiency of TC reduces from 82% to 32% in the presence of TEMPOL, while it decreases from 82% to 65% and to 72% after the addition of EDTA-2Na and IPA, respectively. Thus, $\bullet O_2^-$ is the major reactive specie in the photocatalytic reaction of TpMa/CN, while h^+ and •OH have a slightly positive contribution to the degradation process. ESR analysis was further employed to recognize the active species generated in the photocatalytic process. Herein, DMPO was employed as a spin probe of •OH and $\bullet O_2^-$ in water and methanol, respectively, and the results are depicted in Fig. 6c-d and Fig. S12. Obviously, no ESR signals can be detected in the dark both for CN and TpMa/CN-5. In contrast, distinct characteristic signals are observed upon visible light irradiation, and the TpMa/CN-5 photocatalyst shows a stronger signal than CN, indicating the increased generation of $\bullet O_2^-$. Similarly, the trend of DPMO-•OH signal is consistent with $\bullet O_2^-$. However, considering the standard redox potential of $OH^-/\bullet OH$ (1.99 eV) or $H_2O/\bullet OH$ (2.37 eV) [43–44], the more negative VB potential of CN (1.92 eV) and TpMa (1.72 eV) demonstrates that the sample cannot oxidize OH^- or H_2O to •OH under the visible light irradiation. Thus, •OH may obtain from the reduction of $\bullet O_2^-$ ($\bullet O_2^- + e^- + 2H^+ \rightarrow H_2O_2$, $H_2O_2 + e^- \rightarrow OH^- + \bullet OH$). Then, NBT transformation experiments were further performed to evaluate the amount of superoxide radicals generated in the photocatalytic process. The intensity of NBT characteristic absorption peak (260 nm) significantly decreases in the CN and TpMa/CN-5 samples as time prolongs, implying that $\bullet O_2^-$ acts as the major reactive species to participate in the photocatalytic reaction (Fig. 7a-b). As shown in Fig. 7c, TpMa/CN-5 presents the higher degradation efficiency for NBT and the related *k* value is about 6.5 times higher than that of CN, resulting from an enhanced $\bullet O_2^-$ production. Accordingly, the average $\bullet O_2^-$ generation rates of TpMa/CN-5 and CN are calculated to be 0.64 and 0.13 μmol L^{-1} min^{-1},

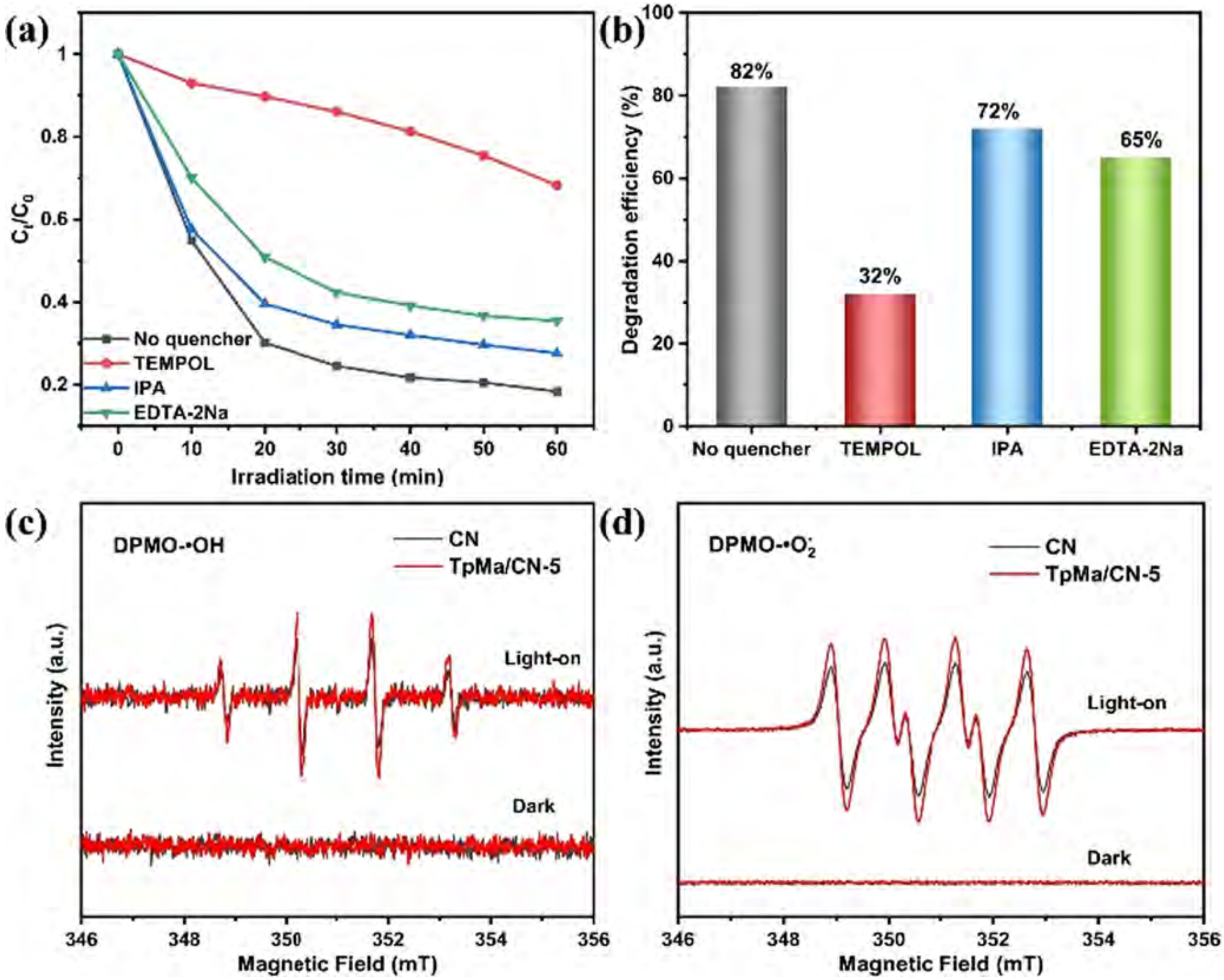

Fig. 6. Photocatalytic degradation curves (a) and degradation efficiencies (b) of TC over TpMa/CN-5 photocatalyst with different quenchers. ESR signals of DMPO-•OH adduct (c) and DMPO-$\bullet O_2^-$ adduct (d) over CN and TpMa/CN-5 systems under visible light irradiation.

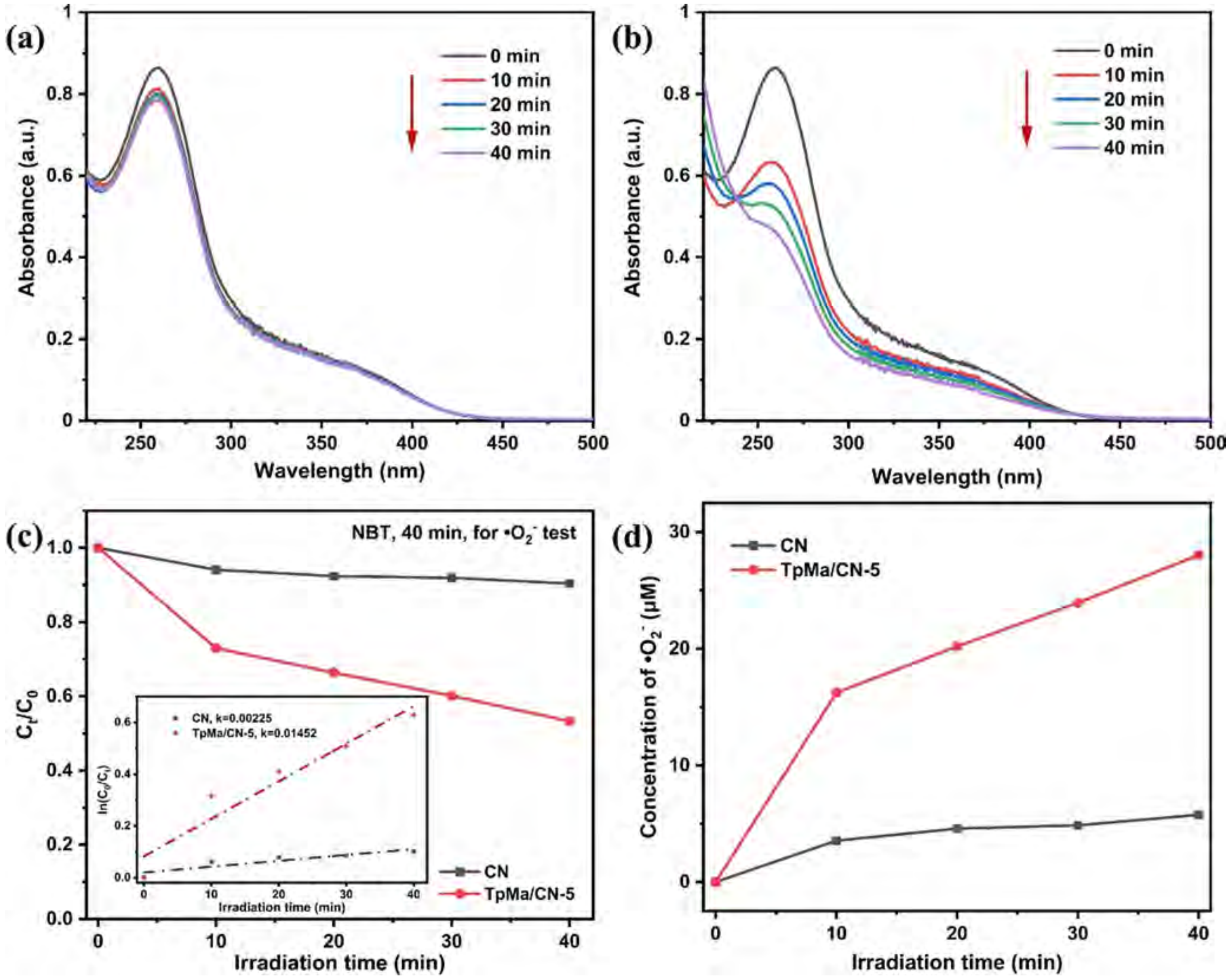

Fig. 7. Absorption curve for NBT solution over (a) CN and (b) TpMa/CN-5 system under visible light irradiation; (c) photodegradation of NBT over the samples and the corresponding pseudo first-order kinetic fitting curves (insert); (d) Time-dependent amount of $\bullet O_2^-$.

respectively (Fig. 7d). These results further verified that TpMa/CN-5 presents an improved photocatalytic activity in $\bullet O_2^-$ formation.

In addition, the as-prepared TpMa/CN heterojunction is also competent to produce H_2O_2, which is an important clean industrial chemical and hydrogen source. As displayed in Fig. 8a, negligible production of H_2O_2 is observed in the existence of CN photocatalysts, indicating the poor photocatalytic activity of CN for H_2O_2 production. As expected, the TpMa/CN heterojunctions show enhanced H_2O_2 production, which is largely dependent on the dosage of TpMa. The highest H_2O_2 production rate is achieved on the TpMa/CN-5 (880.494 μM h^{-1}) under visible-light irradiation, which is about 49 folds as that of CN (17.79 μM h^{-1}). Furthermore, the comparison for H_2O_2 production with other g-C_3N_4-based photocatalysts is provided in Table S4, and TpMa/CN-5 exhibits remarkable activity evaluated by reaction solution, dosage, light source and yield. Control experiments were also conducted to confirm the determinants in the reaction process. As shown in Fig. 8b, limited generation of H_2O_2 is observed without visible light irradiation, indicating the important role of visible light. Similarly, there is no H_2O_2 generation in the absence of photocatalysts, clarifying the indispensable role of photocatalysis. Considering the possibility that the oxidation of water with photogenerated holes could also generate H_2O_2, we replaced O_2 with N_2 and found that the generation of H_2O_2 was greatly decreased. Thus, the generation of H_2O_2 more likely to be the electron reduction of O_2 [45]. Notably, though the amount of H_2O_2 production (556.587 μM) is reduced in the absence of IPA, it is considerable and can compete with other works with the addition of IPA, indicating the great potential of photocatalytic H_2O_2 production without organic charge scavengers.

3.3. DFT calculations

DFT calculations were conducted to get further understanding of the enhanced photocatalytic activities based on the interactions and electronic properties of TpMa/CN heterostructure. Fig. 9a demonstrates the side view of the simulated model of TpMa/CN heterostructure. Band structures of bulk CN and TpMa were simulated via GGA-PBE exchange–correlation functional (Fig. S13). The Fermi level indicated by dot line is set at zero. As displayed in Fig. S13a, the conduction band minimum (CBM) of CN locates at Γ point, while the valence band maximum (VBM) of CN occurs between M and K points, indicating an indirect band gap feature of CN, and the related band gap is 2.25 eV. In contrast to CN, TpMa has the characteristics of the direct band gap with the CBM and VBM lay on the M point, and the calculated band gap is 1.52 eV

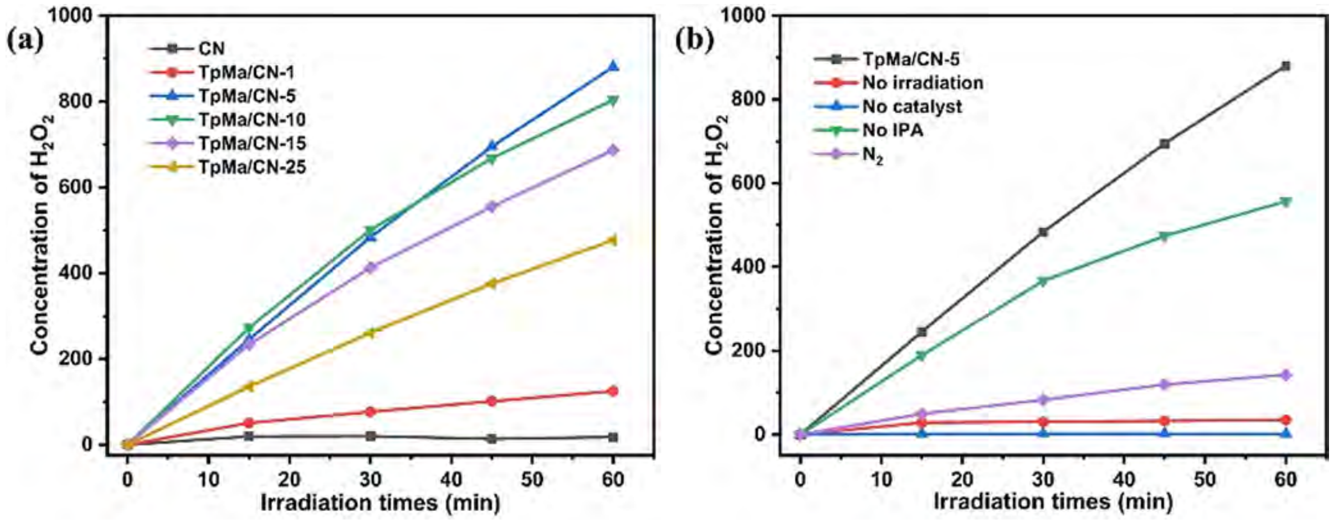

Fig. 8. (a) Photocatalytic production of H_2O_2 under visible light irradiation over different samples; (b) Control experiments for photocatalytic production of H_2O_2 over TpMa/CN-5 sample.

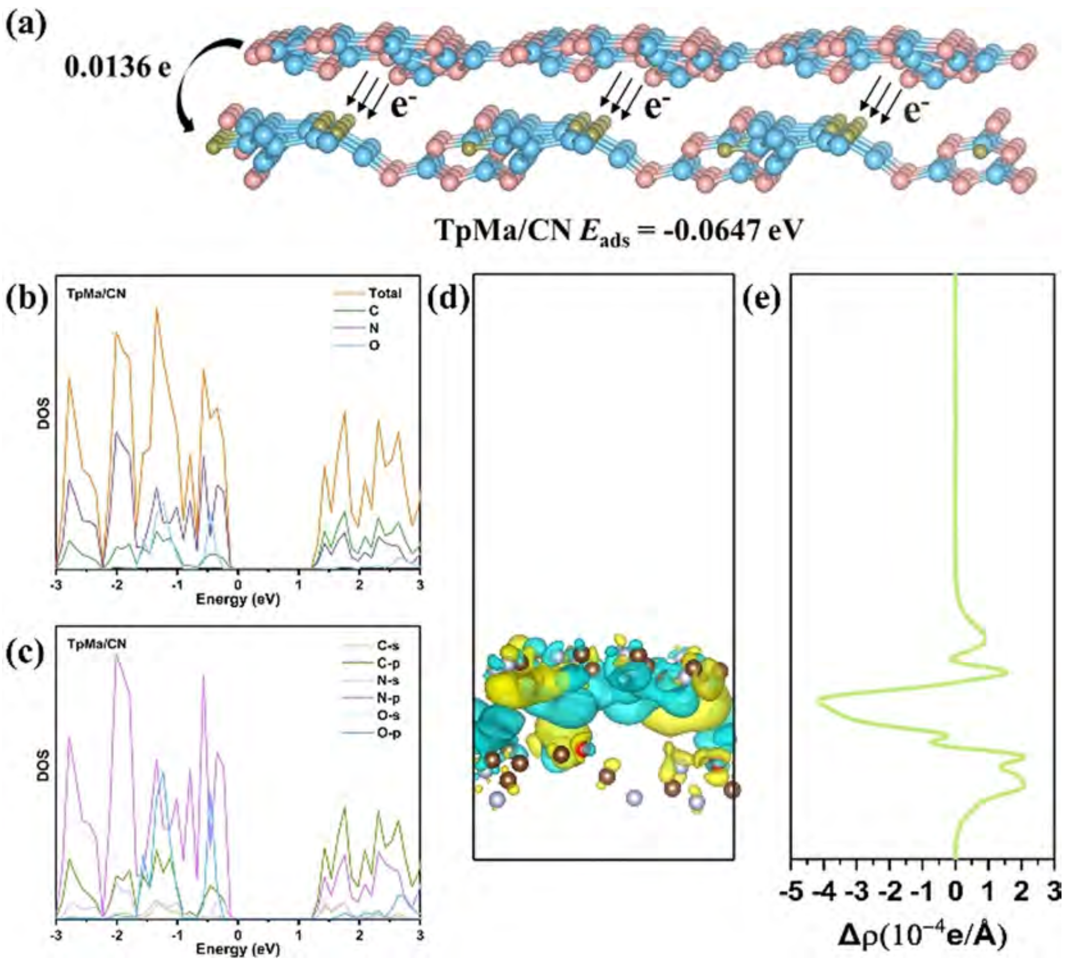

Fig. 9. (a) The side view and the calculated Bader charges of TpMa/CN heterostructure; (b) Total DOS and DOS for elements of TpMa/CN heterostructure; (c) DOS for orbitals of TpMa/CN heterostructure; 3D charge density difference (d), and planar averaged charge density difference (e) of TpMa/CN heterostructure.

(Fig. S13b). Both the computational band gap of CN and TpMa underestimate the experimental results (2.47 eV and 2.32 eV, respectively), which could be ascribed to the inherent lack of derivative discontinuity and delocalization error [46].

Moreover, the density of states (DOS) of CN, TpMa and TpMa/CN were calculated. As shown in Fig. 9b and Fig. S14, the incorporation of TpMa causes the downward shift of CB and results in the narrower bandgaps compared to the pristine CN, indicating that it is

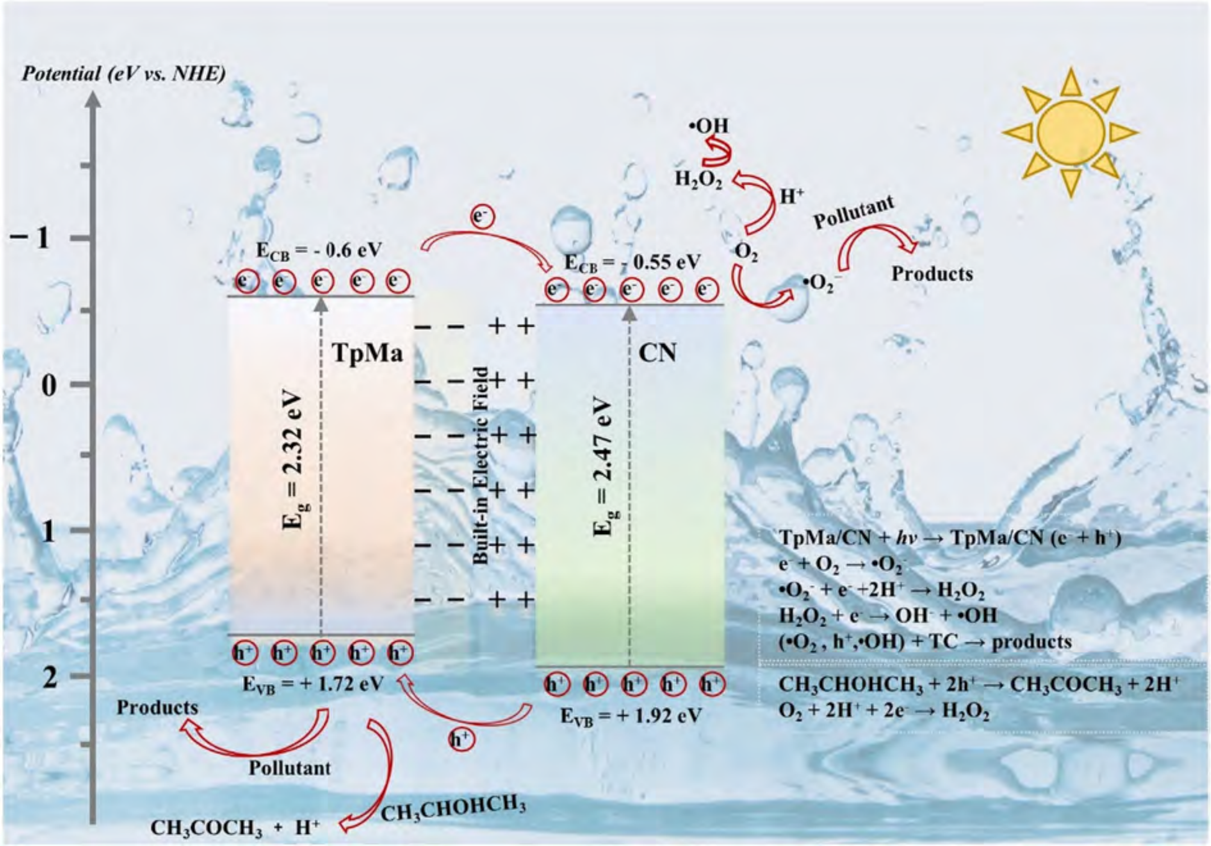

Scheme 2. Schematic illustration of photocatalytic mechanism for TpMa/CN composite under visible light irradiation.

easier to transfer electrons from the VB to the CB under light irradiation. The corresponding DOS for orbitals is demonstrated in Fig. 9c and Fig. S14c-d. N p-orbitals constitute the VB of pristine CN, while p-orbitals of C and N make up the CB. After the introduction of TpMa, apart from N p-orbitals, additional O p-orbitals are found to participate the VB composition, which is originated from the electron-donor units in TpMa.

The 3D charge density difference was further analyzed to uncover the charge transfer and redistribution at the interface of TpMa and CN, based on the follow definition:

$$\Delta\rho = \rho TpMa/CN - \rho TpMa - \rho CN \qquad (3)$$

where ρTpMa/CN, ρTpMa, and ρCN represents the charge densities of the composite, in the same configuration, respectively. The results are described in Fig. 9d, and the charge accumulation and depletion are reflected by the yellow region and the green region, respectively. Obviously, both TpMa and CN undergo charge redistribution at the interface. The planar averaged charge density difference along the Z axis of the TpMa/CN heterostructure (Fig. 9e) directly reveals that the interfacial electron transfer occurs from CN layer to TpMa layer. Especially, the oxygen atoms within Tp play important role to act as the transfer sites. Therefore, a built-in electric field with the direction from the CN surface to the TpMa surface is formed, compelling the swift separation of photo-induced carriers. Additionally, the effective net charge transfer between TpMa and CN was investigated based on the Bader method. As a result, there are 0.014 electron transfers from CN to TpMa (Table S5).

3.4. Photocatalytic mechanisms

Based on the above analysis, a possible mechanism of the enhanced photocatalytic performance for the TpMa/CN heterojunction is put forward (Scheme 2). Before contact, the band edge position of TpMa and CN are different. The CB and VB position of TpMa are more negative than that of CN. Once TpMa and CN are brought together in contact, the type II heterojunctions are formed. As demonstrated above, with the interfacial interaction, a built-in electric field is formed and orients from the CN surface to TpMa surface. Upon the visible-light irradiation, CN and TpMa both generate photoexcited electron-hole pairs on the corresponding CB and VB. Driven by the built-in electric field at the interface and the type II band structures, the photogenerated electrons of TpMa can be rapidly transferred to the CB of CN, and then convert molecular oxygen to $•O_2^-$, considering the negative CB position (−0.55 eV vs NHE) of CN as compared with the redox potential of $O_2/•O_2^-$ (−0.33 eV vs NHE), which could attack and oxidize TC. The left photogenerated holes are accumulated on the surface of TpMa, participating into photocatalytic reactions. Notably, as for H_2O_2 production, IPA trapped holes to provide hydrogen proton (H^+), thereby reacting with oxidative $•O_2^-$ to produce H_2O_2. Noteworthily, driving by the built-in electric field, the photo-induced carriers separate and migrate effectively, which enables more electron-hole pairs participate in the photocatalytic reaction, thereby improving the photocatalytic activity of TpMa/CN heterostructure.

4. Conclusion

In conclusion, donor–acceptor conjugated TpMa was successfully self-assembled onto g-C_3N_4 via π-π interaction. The as-prepared TpMa/CN heterojunctions showed enhanced photocatalytic activity towards TC degradation and green production of H_2O_2 as compared with pristine g-C_3N_4. TpMa/CN-5 showed the highest photocatalytic activity with a TC degradation of 82% and a H_2O_2 production of 880.494 μM after 60 min irradiation. Notably, TpMa/CN-5 exhibited excellent photocatalytic performance as compared to other representative g-C_3N_4-based photocatalysts (Table S3 and Table S4) [47–48]. Experimental data and DFT calculations were comprehensively applied to uncover the reasons including that (i) the introduction of TpMa could broaden the visible-light absorption range of CN, which indicates more effective utilization of sunlight; (ii) the built-in electric field at the interface of TpMa and CN can cause redistribution of charge density and act as the driving force to accelerate the charge carrier separation; (iii) large amounts of active species including $\bullet O_2^-$ and h^+ are generated to promote the photo-oxidation ability. This study demonstrates the important role of built-in electric field for designing g-C_3N_4-based heterojunction photocatalysts and stimulate new inspiration for the utilization of organic photocatalysts for excellent performance in environmental and energy-related applications.

CRediT authorship contribution statement

Han Wang: Conceptualization, Formal analysis, Investigation, Methodology, Visualization, Writing-original draft, Writing-review&editing. **Eydhah Almatrafi:** Visualization, Writing-review&editing. **Ziwei Wang:** Formal analysis, Writing-review &editing. **Yang Yang:** Methodology, Writing-review&editing. **Ting Xiong:** Methodology, Writing-review&editing. **Hanbo Yu:** Formal analysis, Methodology, Writing-review&editing. **Hong Qin:** Formal analysis, Investigation, Writing-review&editing. **Hailan Yang:** Visualization, Writing-review&editing. **Yangzhuo He:** Investigation, Writing-review&editing. **Chenyun Zhou:** Methodology, Writing-review&editing. **Guangming Zeng:** Conceptualization, Formal analysis, Investigation, Methodology, Visualization, Writing-review&editing. **Piao Xu:** Formal analysis, Investigation, Methodology, Visualization, Writing-review&editing.

Declaration of Competing Interest

The authors declare that they have no known competing financial interests or personal relationships that could have appeared to influence the work reported in this paper.

Acknowledgments

This work was supported by the National Natural Science Foundation of China (U20A20323, 51521006, 52070077, 51709101), the Program for Changjiang Scholars and Innovative Research Team in University (IRT-13R17), and the Hunan Provincial Innovation Foundation for Postgraduate (CX20200415).

Appendix A. Supplementary data

Supplementary data to this article can be found online at https://doi.org/10.1016/j.jcis.2021.10.036.

References

[1] Z. Zou, J. Ye, K. Sayama, H. Arakawa, Direct splitting of water under visible light irradiation with an oxide semiconductor photocatalyst, Nature 414 (6864) (2001) 625–627.

[2] Q. Guo, C.Y. Zhou, Z.B. Ma, X.M. Yang, Fundamentals of TiO_2 Photocatalysis: Concepts, Mechanisms, and Challenges, Adv. Mater. 31 (50) (2019), 1901997.

[3] Z. Zhang, Y. Zhu, X. Chen, H. Zhang, J. Wang, A Full-Spectrum Metal-Free Porphyrin Supramolecular Photocatalyst for Dual Functions of Highly Efficient Hydrogen and Oxygen Evolution, Adv. Mater. 31 (7) (2019), 1806626, https://doi.org/10.1002/adma.201806626.

[4] M.L. Marin, L. Santos-Juanes, A. Arques, A.M. Amat, M.A. Miranda, Organic Photocatalysts for the Oxidation of Pollutants and Model Compounds, Chem. Rev. 112 (3) (2012) 1710–1750.

[5] J. Kosco, F. Moruzzi, B. Willner, I. McCulloch, Photocatalysts Based on Organic Semiconductors with Tunable Energy Levels for Solar Fuel Applications, Adv. Energy. Mater. 10 (39) (2020), 2001935, https://doi.org/10.1002/aenm.202001935.

[6] L. Wang, Y. Wan, Y. Ding, S. Wu, Y. Zhang, X. Zhang, G. Zhang, Y. Xiong, X. Wu, J. Yang, H. Xu, Conjugated Microporous Polymer Nanosheets for Overall Water Splitting Using Visible Light, Adv. Mater. 29 (38) (2017), 1702428, https://doi.org/10.1002/adma.201702428.

[7] T. Banerjee, F. Podjaski, J. Kröger, B.P. Biswal, B.V. Lotsch, Polymer photocatalysts for solar-to-chemical energy conversion, Nat. Rev. Mater. 6 (2) (2021) 168–190.

[8] W.J. Ong, L.L. Tan, Y.H. Ng, S.T. Yong, S.P. Chai, Graphitic Carbon Nitride (g-C_3N_4)-Based Photocatalysts for Artificial Photosynthesis and Environmental Remediation: Are We a Step Closer To Achieving Sustainability?, Chem Rev. 116 (12) (2016) 7159–7329.

[9] G. Mamba, A.K. Mishra, Graphitic carbon nitride (g-C_3N_4) nanocomposites: A new and exciting generation of visible light driven photocatalysts for environmental pollution remediation, Appl. Catal. B-Environ. 198 (2016) 347–377.

[10] M.S. Nasir, G.R. Yang, I. Ayub, S. Wang, L. Wang, X.J. Wang, W. Yan, S.J. Peng, S. Ramakarishna, Recent development in graphitic carbon nitride based photocatalysis for hydrogen generation, Appl. Catal. B-Environ. 257 (2019), 117855.

[11] Y. Yang, X. Li, C. Zhou, W. Xiong, G. Zeng, D. Huang, C. Zhang, W. Wang, B. Song, X. Tang, X. Li, H. Guo, Recent advances in application of graphitic carbon nitride-based catalysts for degrading organic contaminants in water through advanced oxidation processes beyond photocatalysis: A critical review, Water Res. 184 (2020), 116200, https://doi.org/10.1016/j.watres.2020.116200.

[12] Q. Liang, Z. Li, Z.-H. Huang, F. Kang, Q.-H. Yang, Holey Graphitic Carbon Nitride Nanosheets with Carbon Vacancies for Highly Improved Photocatalytic Hydrogen Production, Adv. Funct. Mater. 25 (44) (2015) 6885–6892.

[13] C. Zhou, P. Xu, C. Lai, C. Zhang, G. Zeng, D. Huang, M. Cheng, L. Hu, W. Xiong, X. Wen, L. Qin, J. Yuan, W. Wang, Rational design of graphic carbon nitride copolymers by molecular doping for visible-light-driven degradation of aqueous sulfamethazine and hydrogen evolution, Chem. Eng. J. 359 (2019) 186–196.

[14] Z.-F. Huang, J. Song, L. Pan, Z. Wang, X. Zhang, J.-J. Zou, W. Mi, X. Zhang, L.i. Wang, Carbon nitride with simultaneous porous network and O-doping for efficient solar-energy-driven hydrogen evolution, Nano Energy 12 (2015) 646–656.

[15] Z.W. Wang, H. Wang, Z.T. Zeng, G.M. Zeng, P. Xu, R. Xiao, D.L. Huang, X.J. Chen, L.W. He, C.Y. Zhou, Y. Yang, Z.X. Wang, W.J. Wang, W.P. Xiong, Metal-organic frameworks derived $Bi_2O_2CO_3$/porous carbon nitride: A nanosized Z-scheme systems with enhanced photocatalytic activity, Appl. Catal. B-Environ. 267 (2020), 118700.

[16] J. Fu, J. Yu, C. Jiang, B. Cheng, g-C3N4-Based Heterostructured Photocatalysts, Adv Energy Mater 8 (3) (2018), 1701503, https://doi.org/10.1002/aenm.201701503.

[17] J. Chen, C.-L. Dong, D. Zhao, Y.-C. Huang, X. Wang, L. Samad, L. Dang, M. Shearer, S. Shen, L. Guo, Molecular Design of Polymer Heterojunctions for Efficient Solar-Hydrogen Conversion, Adv. Mater. 29 (21) (2017), 1606198, https://doi.org/10.1002/adma.201606198.

[18] H. Wang, H. Wang, Z.W. Wang, L. Tang, G.M. Zeng, P. Xu, M. Chen, T. Xiong, C.Y. Zhou, X.Y. Li, D.N. Huang, Y. Zhu, Z.X. Wang, J.W. Tang, Covalent organic framework photocatalysts: structures and applications, Chem. Soc. Rev. 49 (12) (2020) 4135–4165.

[19] H. Wang, Z.T. Zeng, P. Xu, L.S. Li, G.M. Zeng, R. Xiao, Z.Y. Tang, D.L. Huang, L. Tang, C. Lai, D.N. Jiang, Y. Liu, H. Yi, L. Qin, S.J. Ye, X.Y. Ren, W.W. Tang, Recent progress in covalent organic framework thin films: fabrications, applications and perspectives, Chem. Soc. Rev. 48 (2) (2019) 488–516.

[20] L. Stegbauer, K. Schwinghammer, B.V. Lotsch, A hydrazone-based covalent organic framework for photocatalytic hydrogen production, Chem. Sci. 5 (7) (2014) 2789–2793.

[21] W. Zhong, R. Sa, L. Li, Y. He, L. Li, J. Bi, Z. Zhuang, Y. Yu, Z. Zou, A Covalent Organic Framework Bearing Single Ni Sites as a Synergistic Photocatalyst for Selective Photoreduction of CO_2 to CO, J. Am. Chem. Soc. 141 (18) (2019) 7615–7621.

[22] D. Kong, X. Han, J. Xie, Q. Ruan, C.D. Windle, S. Gadipelli, K. Shen, Z. Bai, Z. Guo, J. Tang, Tunable Covalent Triazine-Based Frameworks (CTF-0) for Visible-Light-Driven Hydrogen and Oxygen Generation from Water Splitting, ACS Catal. 9 (9) (2019) 7697–7707.

[23] M. Luo, Q. Yang, K. Liu, H. Cao, H. Yan, Boosting photocatalytic H-2 evolution on g-C3N4 by modifying covalent organic frameworks (COFs), Chem. Commun. 55 (41) (2019) 5829–5832.

[24] Y. Hou, C.-X. Cui, E. Zhang, J.-C. Wang, Y. Li, Y. Zhang, Y. Zhang, Q. Wang, J. Jiang, A hybrid of g-C3N4 and porphyrin-based covalent organic frameworks via liquid-assisted grinding for enhanced visible-light-driven photoactivity, Dalton T. 48 (40) (2019) 14989–14995.

[25] S. Hu, W. Zhang, J. Bai, G. Lu, L. Zhang, G. Wu, Construction of a 2D/2D g-C3N4/rGO hybrid heterojunction catalyst with outstanding charge separation ability and nitrogen photofixation performance via a surface protonation process, RSC Adv. 6 (31) (2016) 25695–25702.

[26] Q. Li, X.W. Lan, G.Y. An, L. Ricardez-Sandoval, Z.G. Wang, G.Y. Bai, Visible-Light-Responsive Anthraquinone Functionalized Covalent Organic Frameworks for Metal-Free Selective Oxidation of Sulfides: Effects of Morphology and Structure, ACS Catal. 10 (12) (2020) 6664–6675.

[27] S. He, Q. Rong, H. Niu, Y. Cai, Construction of a superior visible-light-driven photocatalyst based on a C_3N_4 active centre-photoelectron shift

platform-electron withdrawing unit triadic structure covalent organic framework, Chem. Commun. 53 (69) (2017) 9636–9639.

[28] M. Bhadra, S. Kandambeth, M.K. Sahoo, M. Addicoat, E. Balaraman, R. Banerjee, Triazine Functionalized Porous Covalent Organic Framework for Photo-organocatalytic E-Z Isomerization of Olefins, J. Am. Chem. Soc. 141 (15) (2019) 6152–6156.

[29] C. Zhou, C. Lai, D. Huang, G. Zeng, C. Zhang, M. Cheng, L. Hu, J. Wan, W. Xiong, M. Wen, X. Wen, L. Qin, Highly porous carbon nitride by supramolecular preassembly of monomers for photocatalytic removal of sulfamethazine under visible light driven, Appl. Catal. B-Environ. 220 (2018) 202–210.

[30] Z. Wei, M. Liu, Z. Zhang, W. Yao, H. Tan, Y. Zhu, Efficient visible-light-driven selective oxygen reduction to hydrogen peroxide by oxygen-enriched graphitic carbon nitride polymers, Energy Environ. Sci. 11 (9) (2018) 2581–2589.

[31] F. Yu, Z. Wang, S. Zhang, H. Ye, K. Kong, X. Gong, J. Hua, H.e. Tian, Molecular Engineering of Donor-Acceptor Conjugated Polymer/g-C_3N_4 Heterostructures for Significantly Enhanced Hydrogen Evolution Under Visible-Light Irradiation, Adv. Funct. Mater. 28 (47) (2018), 1804512, https://doi.org/10.1002/adfm.201804512.

[32] Y. Yang, G.M. Zeng, D.L. Huang, C. Zhang, D.H. He, C.Y. Zhou, W.J. Wang, W.P. Xiong, X.P. Li, B.S. Li, W.Y. Dong, Y. Zhou, Molecular engineering of polymeric carbon nitride for highly efficient photocatalytic oxytetracycline degradation and H_2O_2 production, Appl. Catal. B-Environ. 272 (2020), 118970.

[33] Y. Wang, F. Silveri, M.K. Bayazit, Q. Ruan, Y. Li, J. Xie, C.R.A. Catlow, J. Tang, Bandgap Engineering of Organic Semiconductors for Highly Efficient Photocatalytic Water Splitting, Adv. Energy Mater. 8 (24) (2018), 1801084, https://doi.org/10.1002/aenm.201801084.

[34] C.Y. Zhou, G.M. Zeng, D.L. Huang, Y. Luo, M. Cheng, Y. Liu, W.P. Xiong, Y. Yang, B. Song, W.J. Wang, B.B. Shao, Z.H. Li, Distorted polymeric carbon nitride via carriers transfer bridges with superior photocatalytic activity for organic pollutants oxidation and hydrogen production under visible light, J. Hazard Mater. 386 (2020), 121947.

[35] H. Lv, X. Zhao, H. Niu, S. He, Z. Tang, F. Wu, J.P. Giesy, Ball milling synthesis of covalent organic framework as a highly active photocatalyst for degradation of organic contaminants, J. Hazard Mater. 369 (2019) 494–502.

[36] S. Yu, J. Li, Y. Zhang, M. Li, F. Dong, T. Zhang, H. Huang, Local spatial charge separation and proton activation induced by surface hydroxylation promoting photocatalytic hydrogen evolution of polymeric carbon nitride, Nano Energy 50 (2018) 383–392.

[37] Y. Li, W. Ho, K. Lv, B. Zhu, S.C. Lee, Carbon vacancy-induced enhancement of the visible light-driven photocatalytic oxidation of NO over g-C_3N_4 nanosheets, Appl. Surf. Sci. 430 (2018) 380–389.

[38] M. Luo, Q. Yang, K. Liu, H. Cao, H. Yan, Boosting photocatalytic H_2 evolution on g-C_3N_4 by modifying covalent organic frameworks (COFs), Chem. Commun. 55 (41) (2019) 5829–5832.

[39] B. Zhu, L. Zhang, B. Cheng, J. Yu, First-principle calculation study of tri-s-triazine-based g-C_3N_4: A review, Appl. Catal. B-Environ. 224 (2018) 983–999.

[40] H.B. Yu, J.H. Huang, L.B. Jiang, Y.H. Shi, K.X. Yi, W. Zhang, J. Zhang, H.Y. Chen, X. Z. Yuan, Enhanced photocatalytic tetracycline degradation using N-CQDs/OV-BiOBr composites: Unraveling the complementary effects between N-CQDs and oxygen vacancy, Chem. Eng. J. 402 (2020) 126187–126197.

[41] S. Gao, B. Gu, X. Jiao, Y. Sun, X. Zu, F. Yang, W. Zhu, C. Wang, Z. Feng, B. Ye, Y.i. Xie, Highly Efficient and Exceptionally Durable CO_2 Photoreduction to Methanol over Freestanding Defective Single-Unit-Cell Bismuth Vanadate Layers, J. Am. Chem. Soc. 139 (9) (2017) 3438–3445.

[42] H.B. Yu, J.H. Huang, L.B. Jiang, X.Z. Yuan, K.X. Yi, W. Zhang, J. Zhang, H.Y. Chen, Steering photo-excitons towards active sites: Intensified substrates affinity and spatial charge separation for photocatalytic molecular oxygen activation and pollutant removal, Chem. Eng. J. 408 (2021), 127334.

[43] H. Fu, C. Pan, W. Yao, Y. Zhu, Visible-light-induced degradation of rhodamine B by nanosized Bi_2WO_6, J. Phys. Chem. B 109 (47) (2005) 22432–22439.

[44] L. Yang, G. Dong, D.L. Jacobs, Y. Wang, L. Zang, C. Wang, Two-channel photocatalytic production of H_2O_2 over g-C_3N_4 nanosheets modified with perylene imides, J. Catal. 352 (2017) 274–281.

[45] Y. Zheng, Z. Yu, H. Ou, A.M. Asiri, Y. Chen, X. Wang, Black Phosphorus and Polymeric Carbon Nitride Heterostructure for Photoinduced Molecular Oxygen Activation, Adv Funct Mater 28 (10) (2018), 1705407, https://doi.org/10.1002/adfm.201705407.

[46] P. Mori-Sanchez, A.J. Cohen, W.T. Yang, Localization and delocalization errors in density functional theory and implications for band-gap prediction, Phys. Rev. Lett. 100 (14) (2008), 146401.

[47] H. Zhao, S. Wang, F. He, J. Zhang, L. Chen, P. Dong, Z. Tai, Y. Wang, H. Gao, C. Zhao, Hydroxylated carbon nanotube/carbon nitride nanobelt composites with enhanced photooxidation and H-2 evolution efficiency, Carbon 150 (2019) 340–348.

[48] G.-H. Moon, M. Fujitsuka, S. Kim, T. Majima, X. Wang, W. Choi, Eco-Friendly Photochemical Production of H_2O_2 through O_2 Reduction over Carbon Nitride Frameworks Incorporated with Multiple Heteroelements, ACS Catal. 7 (4) (2017) 2886–2895.